Acta Mech 231, 3387–3404 (2020)
https://doi.org/10.1007/s00707-020-02715-6

ORIGINAL PAPER

D. A. Damasceno · R. K. N. D. Rajapakse · E. Mesquita · R. Pavanello

Atomistic simulation of tensile strength properties of graphene with complex vacancy and topological defects

Received: 22 January 2020 / Revised: 20 April 2020 / Published online: 20 June 2020

Abstract Defects including topological and vacancy defects have been observed in graphene during fabrication. Defects are also introduced to break the lattice symmetry of graphene and thereby obtain enhanced optoelectronic and other properties. It is important that gains in certain properties due to the presence defects are not at the expense of mechanical strength which is important in handling graphene and device fabrication. This paper presents a comprehensive study of the tensile strength and fracture strain of monolayer graphene with commonly observed topological defects and nanopores. Both molecular dynamics and the atomic-scale finite element method (AFEM) are used in this study, and the accuracy of AFEM in simulating complex topological and vacancy defects including line defects is established. It is found that the tensile strength properties have a complex dependency on the defect shape, size, and chirality. Certain defect geometries are found to be mechanically superior to other defect geometries thereby supporting the concept of topological design of graphene to optimize properties. The study also establishes AFEM as an efficient and potential tool for topological optimization of the mechanical behaviour of graphene.

1 Introduction

Graphene is one of the most studied carbon nanostructures due to its extraordinary properties [1]. Top-down and bottom-up synthesis approaches have been used to produce graphene and graphene-based devices [2]. However, it is inevitable that defects are formed during synthesis and fabrication. Defects including topological and vacancy defects have been introduced into graphene to break the lattice symmetry and thereby obtain enhanced optoelectronic and other properties for various practical applications [3,4]. For example, vacancy defects have been introduced to create antidot lattices, which makes graphene a semiconductor with optoelectronic properties [5]. In addition, researchers [6,7] have shown that graphene with vacancy defects such as nanopores has interesting practical applications.

The defects in graphene can be vacancies (missing atoms); topological defects such as Stone–Wales defects [8]; dislocations (line defects) [9]; grain boundaries [10]; impurities; and others [11,12]. The Stone–Wales defects identified as SW1 and SW2 have two pentagons and two heptagons as shown in Fig. 1a–b, respectively. Figure 1c shows a divacancy (DV) defect obtained by removing two atoms from a perfect lattice. In this case,

D. A. Damasceno · R. K. N. D. Rajapakse (✉)
School of Engineering Science, Simon Fraser University, 8888 University Dr, Burnaby, BC V5A 1S6, Canada
E-mail: rajapakse@sfu.ca

R. K. N. D. Rajapakse
Sri Lanka Institute of Information Technology, Malabe, Sri Lanka

E. Mesquita · R. Pavanello
Department of Computational Mechanics and Center for Computational Engineering & Sciences (CCES), University of Campinas, Mendeleyev, 200 - Cidade Universitária, Campinas, SP 13083-860, Brazil

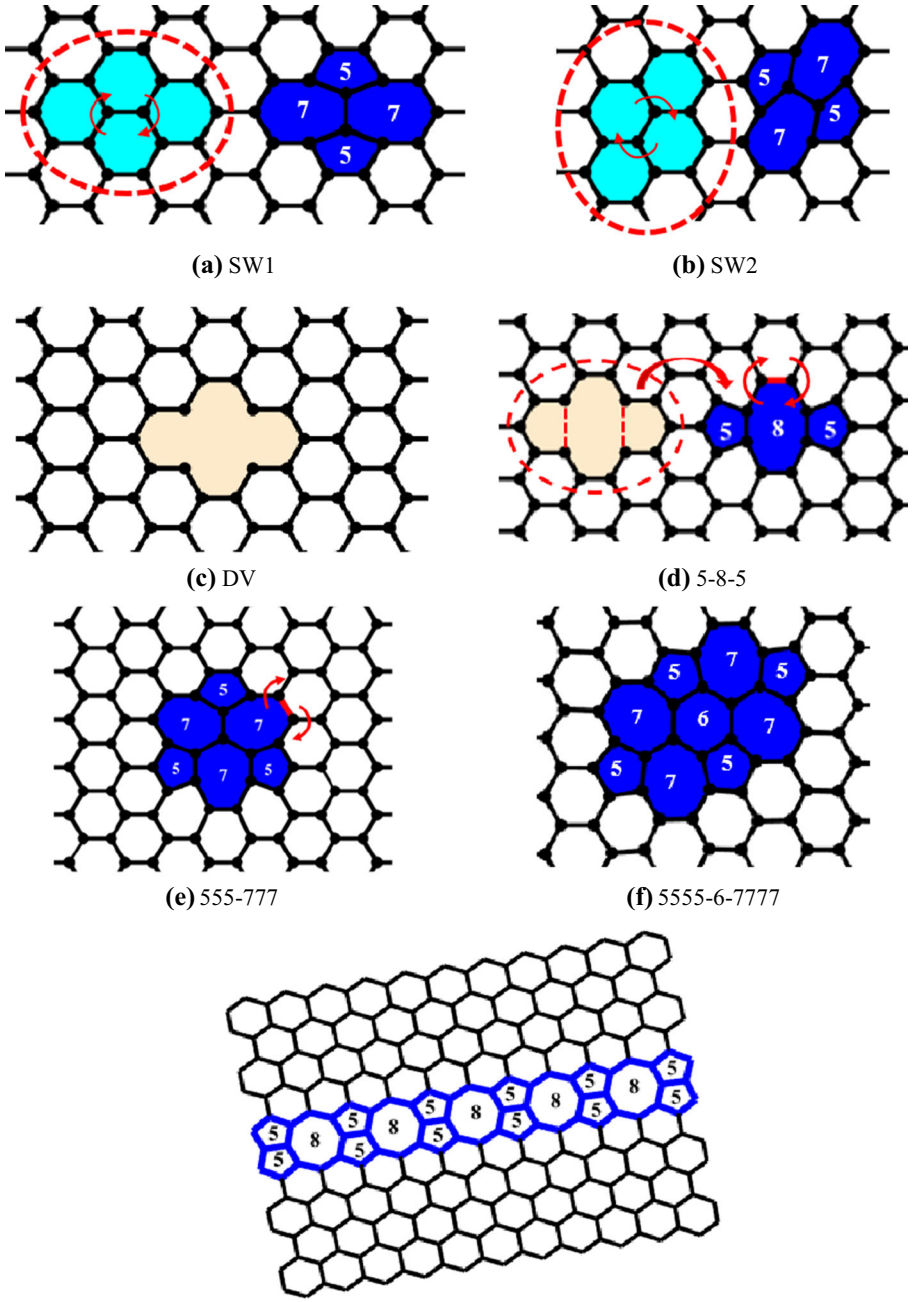

(a) SW1 **(b)** SW2

(c) DV **(d)** 5-8-5

(e) 555-777 **(f)** 5555-6-7777

(g) Line defect

Fig. 1 Defects in graphene

the sp^2 covalent bonds are not maintained. Figure 1d–f shows different patterns of reconstruction of the basic DV defect. The 5-8-5 defect (Fig. 1d) involves two pentagons and one octagon. The rotation of the carbon–carbon bond shown in red by 90° leads to a triple pentagon–triple heptagon (555-777) defect as shown in Fig. 1e. Now, rotating the carbon–carbon bond highlighted in red, a defect identified as 5555-6-7777 (Fig. 1f) is obtained. This defect contains four pentagons, four heptagons, and one hexagon rotated by 30° in relation to the original configuration. All these defect configurations have been experimentally observed [13].

In addition to the basic topological defects shown in Fig. 1a–f, extended line defects (ELD) are another variation of topological defects that are observed in graphene [9,14]. An extended line defect formed by alignment of 5-8-5 defects, as shown in Fig. 1g, has been experimentally observed in graphene along the *zz*

direction [9]. It is a type of grain boundary (GB) with zero rotation angle and yields remarkable electronic properties with interesting applications such as a metallic wire interconnects [9,14]. Souza et al. [15] studied the electronic and transport properties of ELD formed by heptagon–pentagon and octagon–pentagon for gas sensor applications. Other studies focused on the effects of ELD on the electronic and chemical properties of graphene [15,16].

There is also growing interest in the topological design of 2D materials by defects and vacancies to enhance their physical properties. It is, however, important that enhancement of optoelectronic and other properties as confirmed by the studies mentioned above does not happen at the expense of mechanical properties since mechanically weak graphene is hard to manipulate and use in devices. Studies have shown that simple defects have a strong influence on the ultimate tensile strength and failure strain of graphene [17–19]. Liu and Chen [20] performed molecular dynamics (MD) simulations to study the mechanical properties of nanoporous graphene considering different sizes, shapes, and nanopore densities. Lee et. al. [21] used a structural beam element to study the elastic modulus of nanoporous graphene. However, the application of continuum beam models to simulate graphene is questionable. Using MD simulations, the effects SW1, SW2, 5-8-5, 555-777 and 5555-6-7777 defects on Young's modulus of graphene have been examined [22,23]. Existing studies on graphene with defects have considered relatively simple defects and paid limited attention to fracture strength and strain which are important mechanical properties in device design and fabrication.

Both MD simulations and continuum-based methods have been employed to study the mechanical properties of graphene. The applicability of continuum-based methods is questionable. MD solves the dynamic equilibrium equation of an atomic system based on an inter-atomic potential field and has been applied to study graphene with defects [17,22,24–26]. Liu et al. [27] proposed the atomic-scale finite element method (AFEM), which is also based on an inter-atomic potential field, as a computationally efficient alternative to MD. AFEM solves for the final equilibrium state based on the nonlinear static response of the atomic system. AFEM is an order N method compared to MD which is order N^2. It has shown good accuracy for simulation of the mechanical response of graphene [28–31]. However, its application for complex topological and vacancy defects such as those shown in Fig. 1 is not reported in the literature.

Based on the above review of the literature, this paper has two objectives. The first objective is to confirm the accuracy of AFEM in estimating the tensile properties of graphene with complex topological defects by a systematic comparison with MD simulations and position AFEM as a potential tool for topological optimization of graphene. The second objective is to carry out a study on the tensile strength properties of graphene with complex topological defects including line defects and facilitate mechanical design of graphene-based devices and future studies on topological design of 2D materials. The AFEM formulation used in the present study is based on the second-generation reactive empirical bond order (REBO) potential [32]. It is one of the most used potentials for modelling graphene [33]. The MD simulations are based on the LAMMPS [34] software package for atomistic simulations.

2 Atomic-scale finite element method (AFEM)

The formulation of AFEM is briefly described below for completeness. AFEM is formulated based on an inter-atomic potential and the total energy of a system of atoms. The total energy expression, E_{tot}, is formed by the inter-atomic potential, U ,and the work done by an external force, W_{fext}, as presented in Eq. (1) [27],

$$E_{\text{tot}} = U_{\text{tot}} - W_{\text{fext}}, \tag{1}$$

$$U_{\text{tot}} = \sum_{i<j}^{Na} U\left(\underline{x}_j - \underline{x}_i\right); \quad W_{\text{fext}} = \sum_{i=1}^{Na} F^i_{\text{ext}} \underline{x}_i \tag{2}$$

where Na is the number of atoms, F^i_{ext} is the external force acting on atom i, and $\underline{x}_i$ and $\underline{x}_j$ are the positions of the atoms i and j.

The equilibrium configuration of the system is obtained from the total energy minimization with respect to the position, $\underline{x}$, as [27],

$$\frac{\mathrm{d}E_{\text{tot}}}{\mathrm{d}\underline{x}} = 0, \tag{3}$$

The following equilibrium equation is obtained from the Taylor series expansion of the total energy, E_{tot}, around the equilibrium configuration,

$$\left[K(\underline{u})\right]\ \{\underline{u}\} = \left\{P\left(\underline{u}\right)\right\}, \tag{4}$$

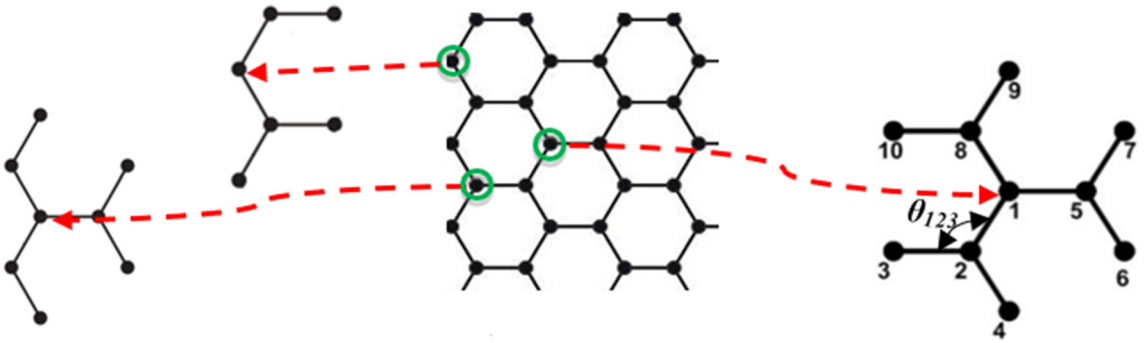

Fig. 2 Atomic finite elements used to model a graphene sheet

where $\{\underline{u}\}$ is the displacement increment vector, $[K(\underline{u})]$and $\{P(\underline{u})\}$ are the nonlinear stiffness matrix and the non-equilibrium force vector, respectively, which depend on the equilibrium position and are expressed as

$$[K(\underline{u})] = \left[\left.\frac{\mathrm{d}^2 E_{\mathrm{tot}}}{\mathrm{d}\underline{x}\mathrm{d}\underline{x}}\right|_{\underline{x}=\underline{x}^{(0)}}\right]; \{P(\underline{u})\} = \left\{-\left.\frac{\mathrm{d}E_{\mathrm{tot}}}{\mathrm{d}\underline{x}}\right|_{\underline{x}=\underline{x}^{(0)}}\right\} \tag{5}$$

The nonlinear equilibrium equation of AFEM given by Eq. (4) is solved iteratively by applying the force control method and the modified Newton–Raphson procedure [35]. In this study, the AFEM is applied based on the second-generation REBO potential [32]. The energy stored in the bond between atoms i and j denoted by $U_{ij}^{\mathrm{second\_REBO}}$ can be expressed as [32]

$$U_{ij}^{\mathrm{second\_REBO}} = f(r_{ij})\left(V_{ij}^{R} + B_{ij}V_{ij}^{A}\right) \tag{6}$$

where V_{ij}^{R} and V_{ij}^{A} are the repulsive attractive functions, $f(r_{ij})$ is the cut-off function, and B_{ij} is known as bond order term, which is related to forming and breaking of the bonds, number of neighbours, and the angle between the atoms. The explicit forms of V_{ij}^{R}, V_{ij}^{A} and $f(r_{ij})$ are given elsewhere [30].

A complete atomic finite element (AFE) based on the second-generation REBO potential has 10 atoms as shown in Fig. 2. The central atom 1 interacts with the first nearest neighbour atoms, 2, 5, and 8, and the second nearest neighbour atoms 3, 4, 6, 7, 9, and 10 by the first neighbour atoms. The atomic configuration of the basic AFE for edge atoms is different from a central atom and involves less than 10 atoms. A description of the five basic AFEs required for edge atoms and atoms around vacancies is described elsewhere [30].

The total energy of atom 1 can be expressed as,

$$U_{\mathrm{tot}}^{1} = \left(U_{12}^{\mathrm{second\_REBO}} + U_{15}^{\mathrm{second\_REBO}} + U_{18}^{\mathrm{second\_REBO}}\right)1/2. \tag{7}$$

In Eq. (7), the energy of the central atom 1 is made of the bond energies of the 1–2, 1–5, and 1–8 bonds as shown in Fig. 2. Note that the effect of the bond energies of the second nearest neighbour atoms (e.g. bond 3–2, 5–6, 8—9, etc.) to the bond energies of the first neighbour atoms is by the bond angle θ which appears in the bond energy expressions of the second-generation REBO potential [30,32]. The details of the expressions for $U_{ij}^{\mathrm{second\_REBO}}$ are given elsewhere [30] and not repeated here for brevity. Equation (7) is repeated for each atom i in the system and added to calculate the total atomic energy of the system. For example, when the energy of the atom 2 is calculated, its total energy is formed by the bond energies of the bonds 2–3, 2–4, and 2–1. It is important to monitor the bond lengths during AFEM modelling to ensure that only the energies of bonds within the cut-off length are considered in computing the bond energy of each atom. The cut-off radius is set as 2.0 Å in this study to avoid non-physical behaviour and overestimating the forces [36]. Several studies have examined the influence of the cut-off radius on MD simulations. The chosen radius is widely used in the literature to achieve stable results for a wide range of problems involving graphene [30,36]. The bond lengths are computed and monitored at each load step and during iterations of the nonlinear equilibrium solver for both nearest neighbour bonds (e.g. 1–2, 1–5, and 1–8) as well as the second nearest neighbour bonds (e.g. 2–3, 2–4, 5–6, 5–7, 8–9, and 8–10) to ensure that bond energies are properly accounted.

3 Results and discussion

3.1 Mechanical response of nanoporous graphene

In a previous article [30], the accuracy of AFEM in modelling graphene nanoribbons (edge effects) has been established. In this paper, we demonstrate the accuracy and application of AFEM to nanoporous graphene and more complex vacancy and topological defects. A pristine graphene sheet with 984 atoms with dimensions of 48.9 Å $\times$ 48.4 Å is used as the base model to create various nanopore configurations by removing selected atoms. The initial bond length between two carbon atoms is taken as 1.396 Å. The tensile loading is applied in one direction, either along the armchair (*ar*) or zigzag (*zz*) directions, on all atoms at one edge, while the opposite edge is fully constrained, as illustrated in Fig. 3a. Five types of nanopore geometries identified as NP1, NP2, NP3, NP4, and NP5 (Fig. 3a–e) are produced by removing selected central atoms in the base model. These nanoporous graphene sheets have interesting practical applications [7,20]. Additionally, the effect of a complex nanoporous geometry on the mechanical behaviour is investigated by introducing multiple (four) nanopores as shown in Fig. 3f. This configuration is identified as NP6. The configurations NP1 to NP6 are analyzed using MD based on the LAMMPS package [34] using the isothermal-isobaric (NPT) ensemble, at temperature 1 K and the AIREBO potential with cut-off radius equal 2.0 Å. Periodic boundary conditions are considered in both directions. The time integration step for the MD simulations is 0.05 fs, and the tension load is applied to the graphene in the *ar* or *zz* directions with a strain rate of 0.001 ps^{-1}.

Figure 4a–b shows a comparison of the stress–strain curves obtained from AFEM with loading along the *ar* and *zz* directions. The nanoporous sheets loaded in both *ar* and *zz* directions show substantial reduction in the strength and failure strain due to the presence of pores compared to a pristine sheet. The stress–strain curves are initially linear and show negligible effect of the defect geometry at very small strains. However, the effect of pore geometry become more significant at higher strains ($> 2\%$). Figure 4c shows a comparison between the stress–strain curves obtained from AFEM and MD for the NP2 and NP3 sheets under tension in the *ar* and *zz* directions. The curves obtained from the two methods agree well up to the failure point confirming the accuracy of AFEM.

Figure 4d–e shows a comparison of the fracture strength and strain obtained from AFEM and MD simulations for the sheets shown in Fig. 3. The results show close agreement between the AFEM and MD simulations with fracture strength slightly underestimated ($< 5\%$) by AFEM and nearly identical fracture strains. AFEM is therefore capable of modelling nanoporous graphene under a wide range of pore geometries and sizes. The armchair sheets are generally weaker and less ductile compared to the zigzag sheets which is due to the orientation of bonds with the loading directions. Note that AFEM solves for the equilibrium configuration at a given load level under static conditions, whereas MD considers the dynamic equilibrium equations and time evolution of bond lengths under loading. As such, some differences between the failure loads and strains from the two schemes are natural. However, the current simulations confirm that AFEM results for all practical purposes are very close to MD results which are obtained at a relatively higher computational cost. For a pristine sheet, the ultimate tensile strength obtained from AFEM is 101 GPa and 116 GPa and the fracture strain is 0.15 and 0.23 along *ar* and *zz* directions, respectively. These results generally agree well with the values reported in the literature, with the range from 83 to 137 GPa, and 0.12 to 0.27 in the *ar* direction, and 98–138 GPa and 0.12 to 0.28 in the *zz* direction [12,37]. Note that the bulk of the results reported in the literature for strength and failure strains corresponds to periodic boundary conditions, and the results for practically useful cases of finite graphene sheets show some difference due to edge effects.

Due to the presence of a NP1 pore, the strength in the *ar* direction is reduced from 101 to 64 GPa and the failure strain from 0.15 to 0.09, while in the *zz* direction the strength reduces from 116 to 88.5 GPa and the strain from 0.23 to 0.14. A comparison of nanopore shapes in Fig. 3 shows that the pore size increases from NP1 to NP5 and the pore boundary pattern is different for each case. It is interesting to note from Fig. 4 that the order of the stress–strain curves does not follow the size of the pore. For example, NP3 and NP5 are stronger and more ductile than NP2 and NP4, respectively, and NP4 is the weakest configuration in the *zz* direction. However, in the *ar* directions these patterns are changed with NP5 as the weakest configuration followed closely by NP3, and the response of NP2 is very close to NP1, while NP4 is between to NP2 and NP3.

In general, NP6 with multiple pores has a similar ductility as NP1 in both loading directions, but much higher ductility compared to other pore configurations in the *zz* direction. Strength of NP6 is slightly higher than NP5 in the *ar* direction but lower than the sheets with other pore configurations. However, the strength of NP6 in the *zz* direction is quite closer to the strengths of NP2, NP4, and NP5. Note that NP6 is a configuration

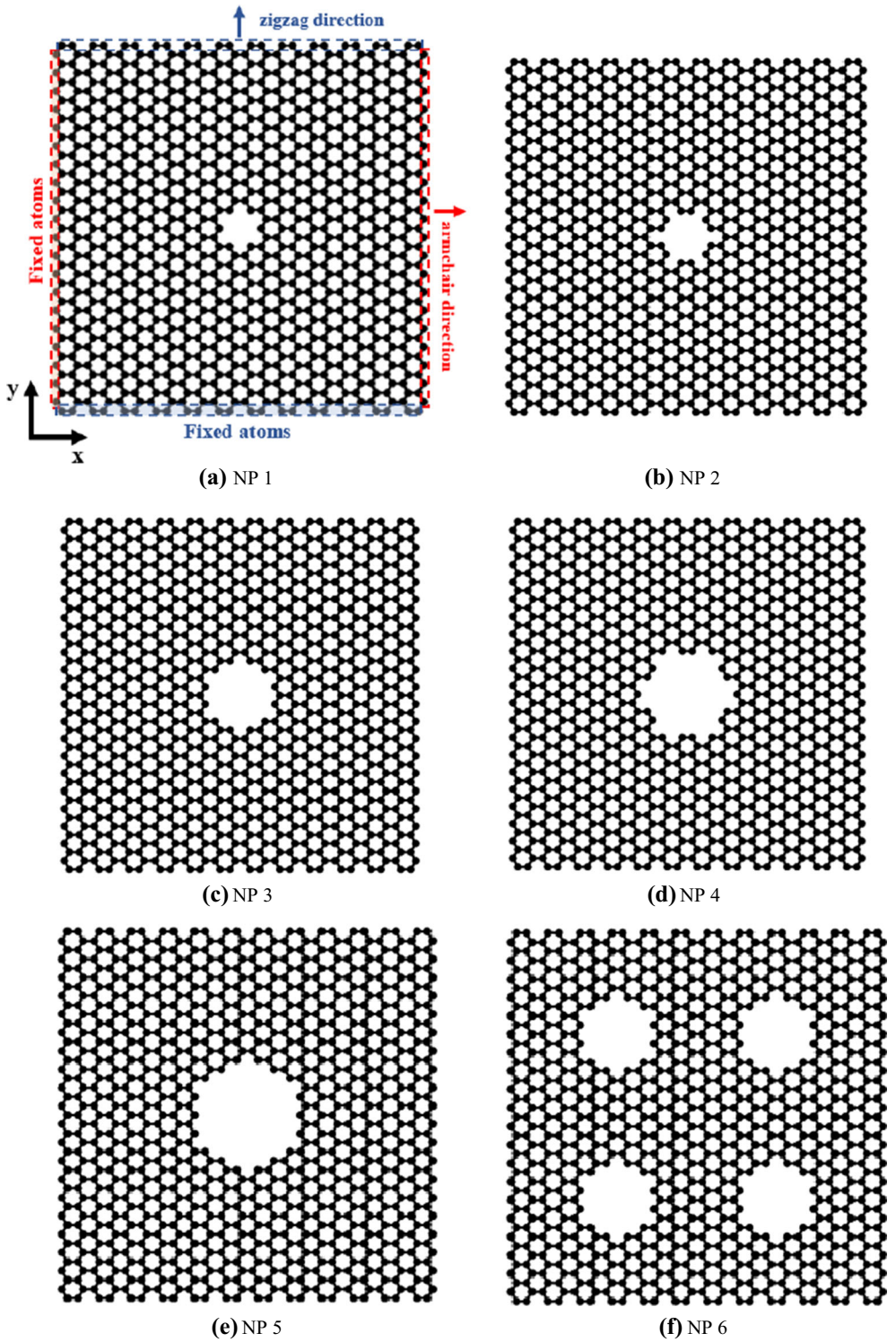

Fig. 3 Nanopore geometries considered in modelling

formed by multiple (four) nanopores of NP3 type. Considering this fact, it is interesting to note that in both loading directions NP6 is more ductile than NP3 although NP3 is about 15% and 7% stronger than NP6 in the *ar* and *zz* directions, respectively. The fact that the highly porous configuration of NP6 in the *zz* direction is as

ductile as N1 and as strong as other porous configurations except N1 and N3 implies that it could be used for interesting nanofluidic applications in engineering disciplines.

The behaviour observed in Fig. 4 indicates that the mechanical response of nanoporous graphene has a complex relationship with the pore size and the pore boundary atomic arrangement. A closer look shows that NP1, NP3, and NP5 have similar pore boundary atomic arrangements (primarily armchair-type configuration) with increasing pore size. Therefore, the stress–strain curves follow a similar order. However, the pore boundary atomic arrangements of NP2 and NP4 are similar but different from NP1 and are prone to relatively higher boundary bond breaking. It makes NP4 the weakest followed by NP2. In the case of tensile loading in the *ar* direction, the boundary atomic arrangement is favourable to pore opening in the case of NP1-type pores compared to NP2 which could favour shrinking of the defect and even some bond reformation at the boundary. Therefore, NP2-type pores are stronger than NP3. The trend of the stress–strain curves in the *ar* and *zz* directions obtained from AFEM in Fig. 4a–b is similar to the trend found by Liu and Chen [20], except for the case of NP5 in the *zz* direction, which was between NP2 and NP4. This difference could be due to the different size of graphene sheet and other factors such as temperature and periodic boundary conditions.

3.2 Mechanical response of graphene sheets with complex topological defects

In this section, we focus on the topological defects shown in Fig. 1. Graphene sheets with dimensions of 48.9 Å × 48.4 Å are used in the modelling. Each sheet has a single defect of the configurations shown in Fig. 1a–f located in its central region, as illustrated in Fig. 5. The topological defects break the perfect hexagonal lattice of graphene, while the sp^2 covalent bonds are maintained. In the case of the DV defect, the sp^2 covalent bonds are not maintained due to missing atoms, thereby some atoms are connected to less than three neighbouring atoms. The bond lengths are also different for certain atoms compared to a perfect lattice, specially the rotated carbon–carbon bonds.

Figure 6 shows a comparison between the stress–strain curves obtained from AFEM and MD for sheets with the six types of defects under tension along the *ar* and *zz* directions. Figure 6a presents the AFEM results for SW1 defect, and there is good agreement between the AFEM and MD simulations. Based on the AFEM calculation, the fracture stress is 102.5 GPa and the failure strain is 0.17 in the *zz* direction, while in the *ar* direction the fracture stress is 72 GPa and the failure strain is 0.1. These results generally agree well with the values reported in the literature for strength and fracture strain [24,25,38–40], which range from 90 to 107.6 GPa and 0.13–0.18 in the *zz* direction, and 12.25–103.7 GPa and 0.013–0.15 in the *ar* direction. Figure 6b presents the curves for SW2 defect. As shown, the results agree well with MD for both *ar* and *zz* directions. The fracture stress is 88.5 GPa and 74.1 GPa, and the failure strain 0.13 and 0.1 in the *zz* and *ar* directions, respectively. Similar to the case of nanopores, graphene sheets subjected to loading in the *zz* direction show more ductility and higher strength compared to same sheets loaded in the *ar* direction for SW1 and SW2 defects. A sheet with SW1 defect loaded in the *zz* direction is stronger than a similar sheet with a SW2 defect. However, SW1 and SW2 sheets loaded in the *ar* direction have nearly identical stress–strain curves.

Figure 6c and d presents the validation of AFEM with MD for the DV and 5-8-5 defects. Good agreement between the AFEM and MD-based stress–strain curves is noted in both *ar* and *zz* directions. The general trend of the stress–strain curves is similar to the case of Stone–Wales defects, but sheets with the DV and 5-8-5 are less ductile and weaker compared to SW1 defects loaded in the *zz* direction. In the past, AFEM has been applied to model single or double vacancy defects [18], and the fracture strength and the failure strain were reported as 74.7 GPa and 0.1 along the *zz* direction, respectively, for a DV defect. These results are about 15% lower than the values found in this study. The difference between the two studies is primarily due to the different potential functions used in the simulation. In the previous study [18], the Tersoff–Brenner potential was considered. However, it has deficiencies as reported by Brenner et al. [32]. It does not have a double bond or conjugate bond rotation barrier to prevent certain unrealistic bond rotations. In this study, we consider the second-generation REBO potential, which is one of the most established potentials for modelling graphene fracture [33]. In the case of the 5-8-5 defect, strength in the *ar* direction is reduced from 101 to 64.3 GPa and the failure strain from 0.15 to 0.08, while in the *zz* direction the strength reduces from 116 to 86.2 GPa and the strain from 0.23 to 0.13. Using MD, Kochnev et al. [41] found the fracture strength to be 69 GPa in the *ar* direction and 92 GPa in the *zz* direction, which agree well with the current results. These results confirm the accuracy of AFEM for modelling basic topological defects.

Although considerable research has been devoted to study the effects of defects on the mechanical properties of graphene, no past studies have considered the effects of 555-777 and 5555-6-7777 defects on the mechanical

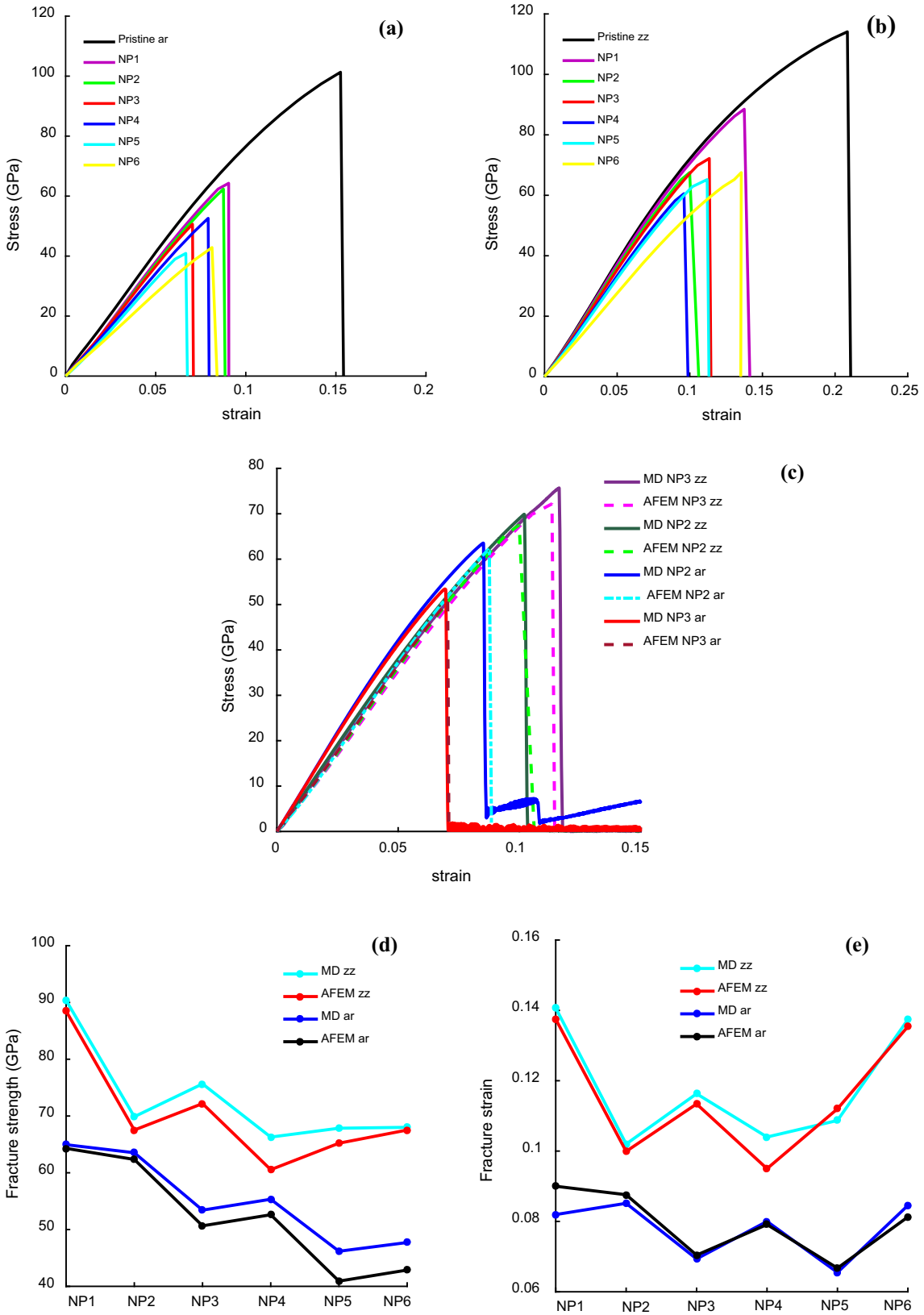

Fig. 4 **a**, **b** Stress–strain curves along *ar* and *zz* directions based on AFEM, **c** comparison of stress–strain curves for NP2 and NP3 obtained from AFEM and MD, **d** comparison of fracture strength, and **e** comparison of fracture strain

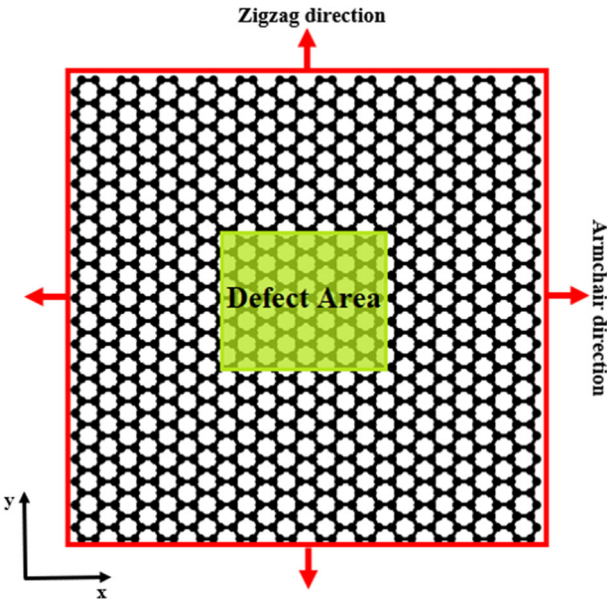

Fig. 5 Schematic sample of graphene with the loading directions and defect area

response. The stress–strain curves shown in Fig. 6e and f for these defects are obtained from AFEM and MD and show good agreement except in the case of fracture strain of a 555-777 defect loaded in the *zz* direction. As mentioned before, we believe this difference is mainly due to the quasi-static nature of AFEM compared to MD, which solves a transient problem accounting for evolution of bond breaking and reforming. Nevertheless, the strength solutions agree within 10%. For a 555-777 defect, the fracture stress obtained from AFEM is 84 GPa and the failure strain is 0.12 in the *zz* direction, while in the *ar* direction the fracture stress is 74.1 GPa and the failure strain is 0.1. In the case of a 5555-6-7777 defect, the fracture stress is 83.8 GPa and the failure strain is 0.12 in the *zz* direction, while in the *ar* direction the fracture stress is 80 GPa and the failure strain is 0.11. In general, as in the case of Fig. 4, the results show good agreement between the AFEM and MD simulations with fracture strength and strain slightly underestimated/overestimated ($< 10\%$) by AFEM except for a 555-777 defect loaded in the *zz* direction.

Figure 7a–b shows a comparison of the fracture strength and strain obtained from AFEM and MD simulations. The defect configurations are numbered from A to F in the same order as shown in Fig. 1 for identification purposes. The results presented in Figs. 6 and 7 clearly show that fracture strength and strain are substantially reduced due to the presence of a topological defect along the *ar* and *zz* directions (pristine sheet: fracture strength 101/116 GPa and fracture strain 0.15/0.23 along the *ar*/*zz* directions, respectively). Like pristine sheets, the sheets with defects are stronger in the *zz* direction (red curves). Reduction in strength and failure strain is the highest for the 5-8-5 defect in the *ar* direction, whereas for the SW1, SW2, DV, and 555-777 defects the reduction in strength and fracture strain in the *ar* direction is quite similar. The 5555-6-7777 defect is the most ductile configuration in the *ar* direction compared to other defects. In the case of loading in the *zz* direction, except for an SW1 defect which is the strongest and most ductile, sheets with other five defects show quite similar tensile strength and fracture strain. The trends seen in Fig. 7 show that the mechanical response of graphene has a complex dependency on the defect shape, chirality and load direction.

It is useful to discuss the fracture patterns of the defects shown in Fig. 1 based on MD. In the case of SW defects loaded in the *zz* direction, reduction in strength is larger for an SW2 defect compared to SW1. This behaviour is related to the tilt angle of the atomic configuration, and an explanation of the influence of different tilt angles for SW defects is given elsewhere [25]. In the case of a DV defect, fracture starts in the bonds around the defect perpendicular to the loading direction. For the six types of defects considered, except for the 5555-6-7777 defect, the failure starts in the bonds around of the defect, such as pentagon–heptagon, pentagon–hexagon, heptagon–hexagon, and octagon–hexagon. In the case of a 5555-6-7777 defect, the failure starts in the bonds shared by hexagon–hexagon parallel to the loading direction, which is similar to the fracture behaviour observed in pristine sheets in the *ar* direction. Therefore, the tensile strength of graphene with a

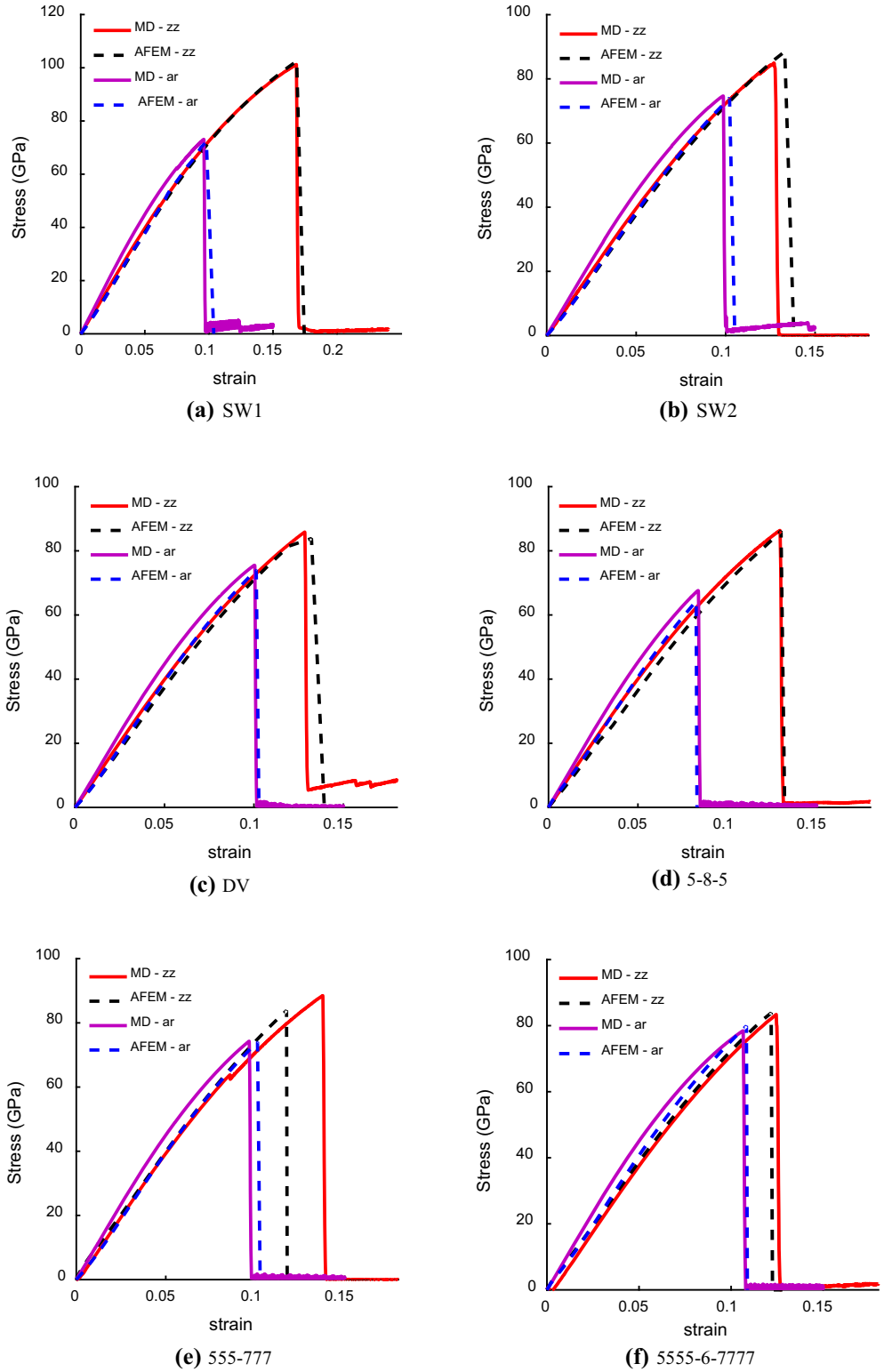

Fig. 6 a–f Stress–strain curves for defects obtained from AFEM and MD

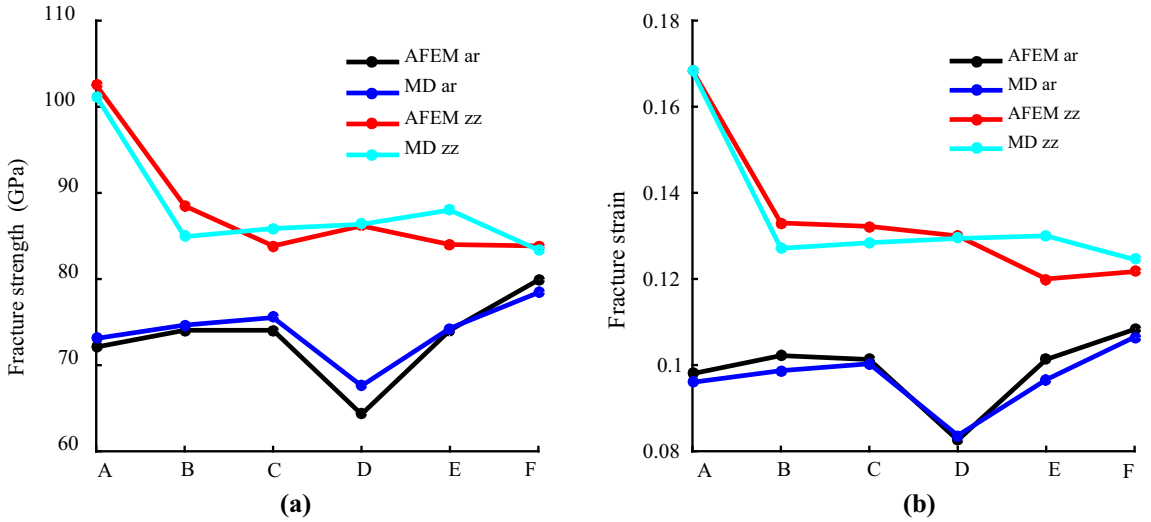

Fig. 7 Comparison of **a** fracture strength, and **b** fracture strain of graphene with topological defects [A-SW1, B-SW2, C-DV, D-5-8-5, E-555-777 and F-5555-6-7777]

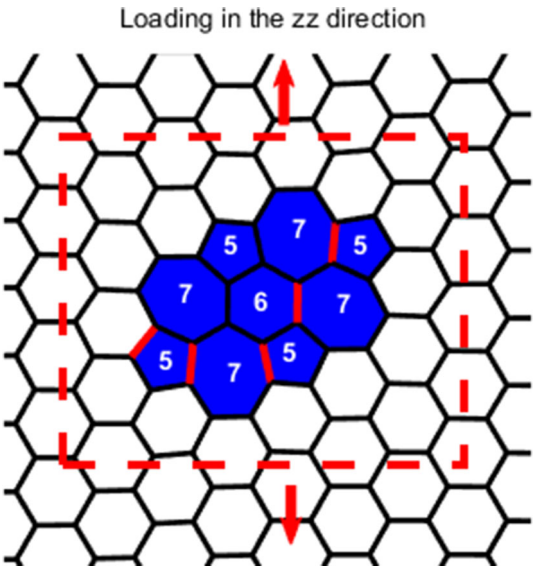

Fig. 8 Graphene sheet with 5555-6-7777 defect used to examine failure mechanisms

5555-6-7777 defect has the smallest deviation from a perfect sheet compared to the other defects due to similar fracture patterns.

In the case of fracture of a sheet with a 5555-6-7777 defect loaded in the *zz* direction, the failure starts in the bonds shared by the pentagon–heptagon, heptagon–hexagon, and pentagon–hexagon bonds (see bonds highlighted in red in Fig. 8. However, unlike the pristine case those highlighted bonds in the *zz* direction are quite parallel to the loading direction, which can lead to the same failure mechanism observed along the *ar* direction for the pristine case. In addition, the same behaviour is observed for sheets with the 5-8-5 and 555-777 defects, where the fracture starts in the bonds around the defect and parallel to the loading direction. Moreover, it is important to note that these defects are obtained by the rotation of two carbon–carbon bonds, as shown in Fig. 1, and the bond length of the rotated carbon–carbon bond is shorter compared to the unrotated, consequently, it is stiffer [10,42].

Figure 9 shows a comparison of the small-strain Young's modulus (E) of pristine graphene and graphene sheets with the topological defects shown in Fig. 1a–f. Each sheet has only one defect located in its central region. The results from AFEM are obtained by calculating the slope of the linear part of stress–strain curves

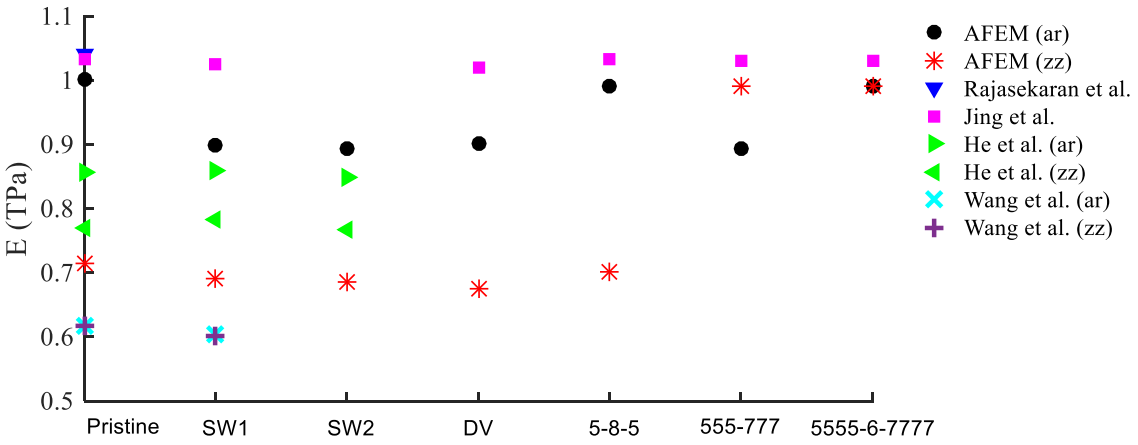

Fig. 9 Comparison of Young's modulus (E) of sheets with different defects (pristine, SW1, SW2, DV, 5-8-5, 555-777 and 5555-6-7777)

(strain range $< 0.5\%$) presented in Fig. 6. The Young's modulus of pristine graphene obtained from AFEM is found to be 1 TPa and 0.71 TPa along the *ar* and *zz* directions, respectively. These values are in a close agreement with the values obtained by Jing et al. [22] and He et al. [25] using molecular dynamics, as shown in Fig. 9. Additionally, these values are also in agreement with the values reported by Rajasekaran et al. [12], Wang et al. [23], Cao [37], and experiments [1].

Comparison of Young's modulus for various topological defects shows interesting trends. For example, E in the *ar* direction is reduced due to SW1, SW2, DV, and 555-777 defects, with sheets showing nearly equal moduli, while the sheets with 5-8-5 and 5555-6-7777 defects show a higher modulus which is very close to the modulus of a perfect sheet. In the *zz* direction, E shows relatively minor changes in the case of SW1, SW2, DV, and 5-8-5 defects, but the 555-777 and 5555-6-7777 defects result in a modulus that is closer to the modulus of a perfect sheet. It has been shown that the addition of topological defects can improve the opto-electronic properties of graphene due to the loss of symmetry in the lattice. A concern with the introduction of defects is the potential loss of stiffness which can affect the mechanical behaviour. However, the results presented in Fig. 9 show that certain defects (e.g. 5555-6-7777) can be introduced in graphene without compromising the stiffness, which is in agreement with the study presented by Jing et al. [22], who concluded using MD simulations that the reconstruction of vacancy defects can help to stabilize Young's modulus.

3.3 Extended line defect (ELD) in graphene

In this section, we study the formation of an extended line of defect (ELD) on the mechanical behaviour of graphene under tension loading by considering ELDs of different lengths. The type of ELD considered in this study is formed by pentagon pairs separated by octagons, identified here as 5-8-5 ELD. To characterize the process of formation of the 5-8-5 ELD, four different ELD sizes are introduced in the centre of a sheet with dimensions of 48.9 Å $\times$ 48.4 Å. Figure 10a shows a basic ELD consisting of two 5-8-5 defects embedded in the centre of the sheet and the boundary conditions. The remaining 5-8-5 ELDs shown in Fig. 10b–d are obtained by adding more 5-8-5 cells. The bond length between two carbon–carbon atoms in a perfect hexagonal lattice is 1.396 Å, but the bond length is different for bonds around defects. The line defects shown in Fig. 10 are labelled as ELD 1 to ELD 4.

Figure 11 shows a comparison of the stress–strain curves obtained from AFEM and MD for ELD 1 with applied loading along the *ar* and *zz* directions. As in the previous cases, the results from the two solution schemes agree well and confirm the ability of AFEM to simulate ELDs as well. A small kink is noted in the MD results in the *ar* direction which is a result of a localized instability due to bond breaking; however, AFEM results show no such kink since the system is globally stable and the solution is based on a quasi-static system. The sheets are more ductile and stronger in the *zz* direction compared to the *ar* direction similar to the sheets with defects considered previously.

Figure 12 shows the stress–strain curves for ELD 1 to ELD 4 based on AFEM. Like the topological and vacancy defects, the presence of 5-8-5 ELDs causes a substantial reduction in tensile strength and failure strain

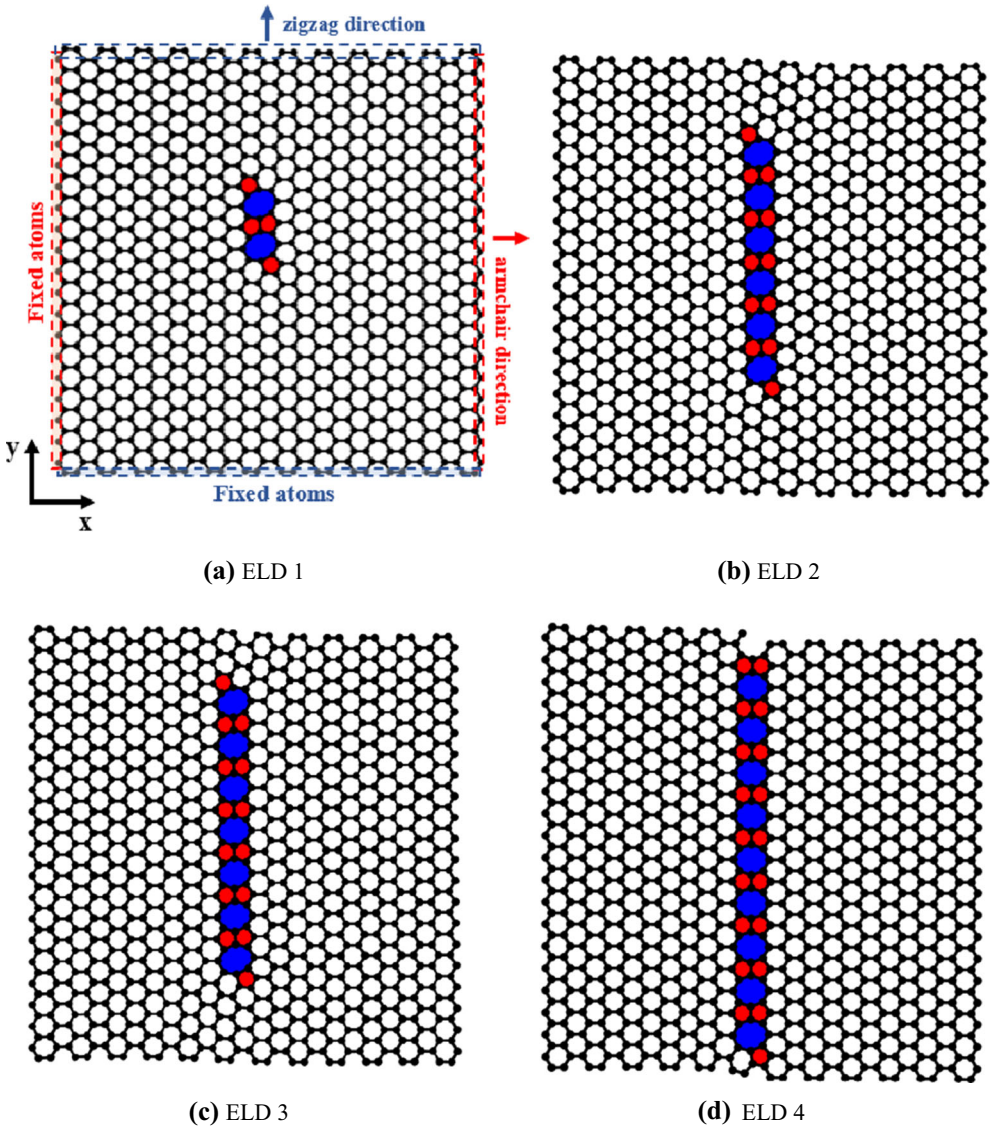

(a) ELD 1 **(b)** ELD 2

(c) ELD 3 **(d)** ELD 4

Fig. 10 Set of 5-8-5 extended line defects

in graphene for both loading directions as shown in Fig. 12. It is interesting to note that under the loading in the *ar* direction the stress–strain curves of the four ELDs show minor dependency on the length of the defect, whereas the length dependency is higher in the case of the loading in the *zz* direction. Graphene sheets loaded in the *zz* direction become more ductile and stronger as the defect length increases; however, the strength and failure strain of a sheet with a defect across the whole length are well below the tensile properties of a perfect sheet. The reduction in the strength observed in Fig. 12 for ELD 4 agrees with the results of Berger and Ratsch [43] who used ab initio modelling to study a similar defect formed by pentagon–octagon and reported the ultimate strength as 91.7 GPa in the *zz* direction.

In order to study the behaviour observed in Fig. 12, we use Fig. 13 to discuss the failure mechanism observed in the visual molecular dynamics package [44] during the MD simulations for the ELD 1 configuration. Fracture in the *ar* direction starts by breaking bonds shared by a pentagon–octagon (bonds highlighted in red in Fig. 13). After one bond breaks, the fracture propagates through the line of defect. Moreover, it is important to mention that no significant out-of-plane displacement is observed during stretching in the *ar* direction. Therefore, along the *ar* direction the number of aligned 5-8-5 defects basically does not interfere with the mechanical response, which confirms the behaviour shown in Fig. 12.

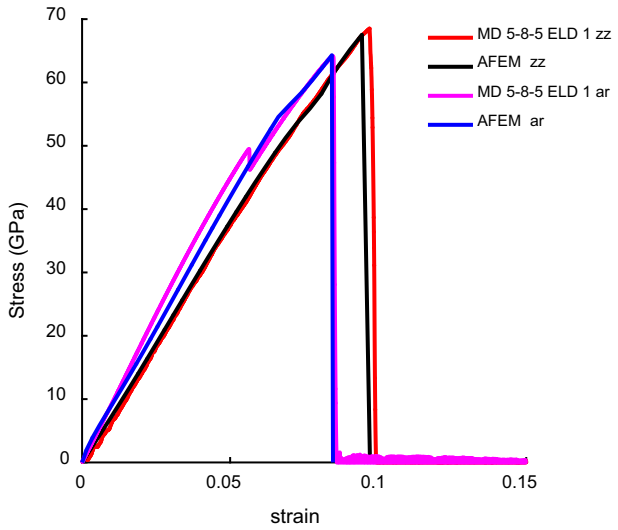

Fig. 11 Comparison of AFEM and MD stress–strain curves for ELD1

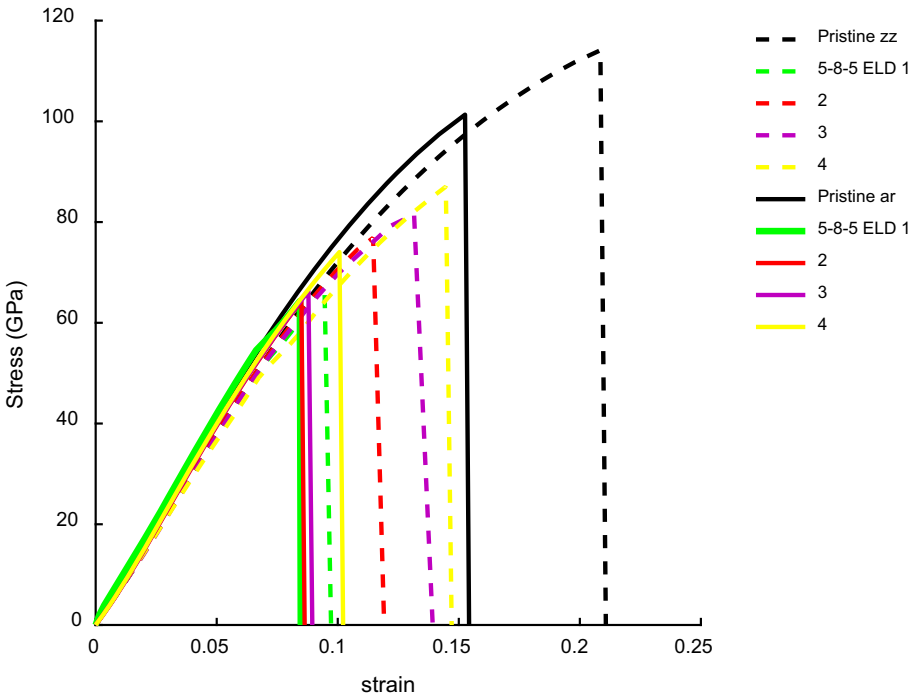

Fig. 12 Stress–strain curves for ELD1 to ELD4 obtained from AFEM

We use Figs. 14 and 15 to discuss the failure mechanisms observed during MD simulations for sheets with ELD 1 and ELD 3 and loaded in the *zz* direction. Figures 14a and 15a show the out-of-plane displacement (i.e. displacement in the z-direction in Ångstroms (Å)) at the initial equilibrium configurations of unloaded sheets with ELD1 and ELD3, respectively. Note the substantial rippling of the sheet around the defect. Orientations of the ripples are different for the two defects, but the peak displacements are in the same range. ELD3 shows negligible out of plane displacement along the defect line, but ELD1 shows substantial troughs ahead and behind the defect line. The importance of out-of-plane displacements due to defects and the potential use of defects and resulting out-of-plane displacements to create novel features and strengthening mechanisms in graphene have been discussed elsewhere [45].

Figures 14b–d and 15b–f show the out-of-plane displacement distributions at various strain levels during loading for ELD1 and ELD3, respectively. Under the applied loading, the ripples of the sheet become aligned

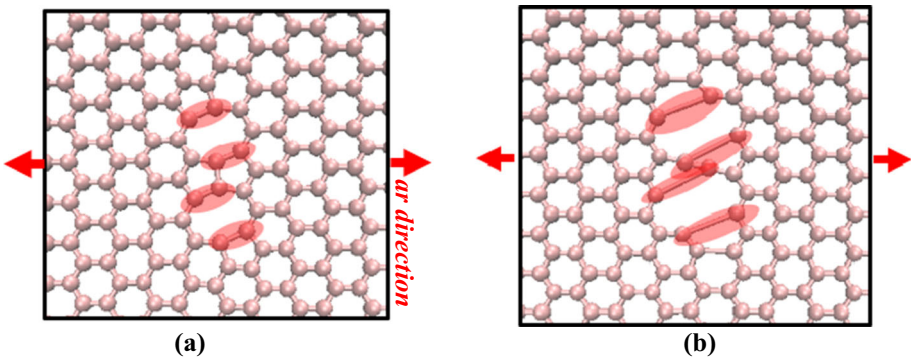

Fig. 13 Failure patterns of a sheet with ELD 1 for loading along *ar* direction

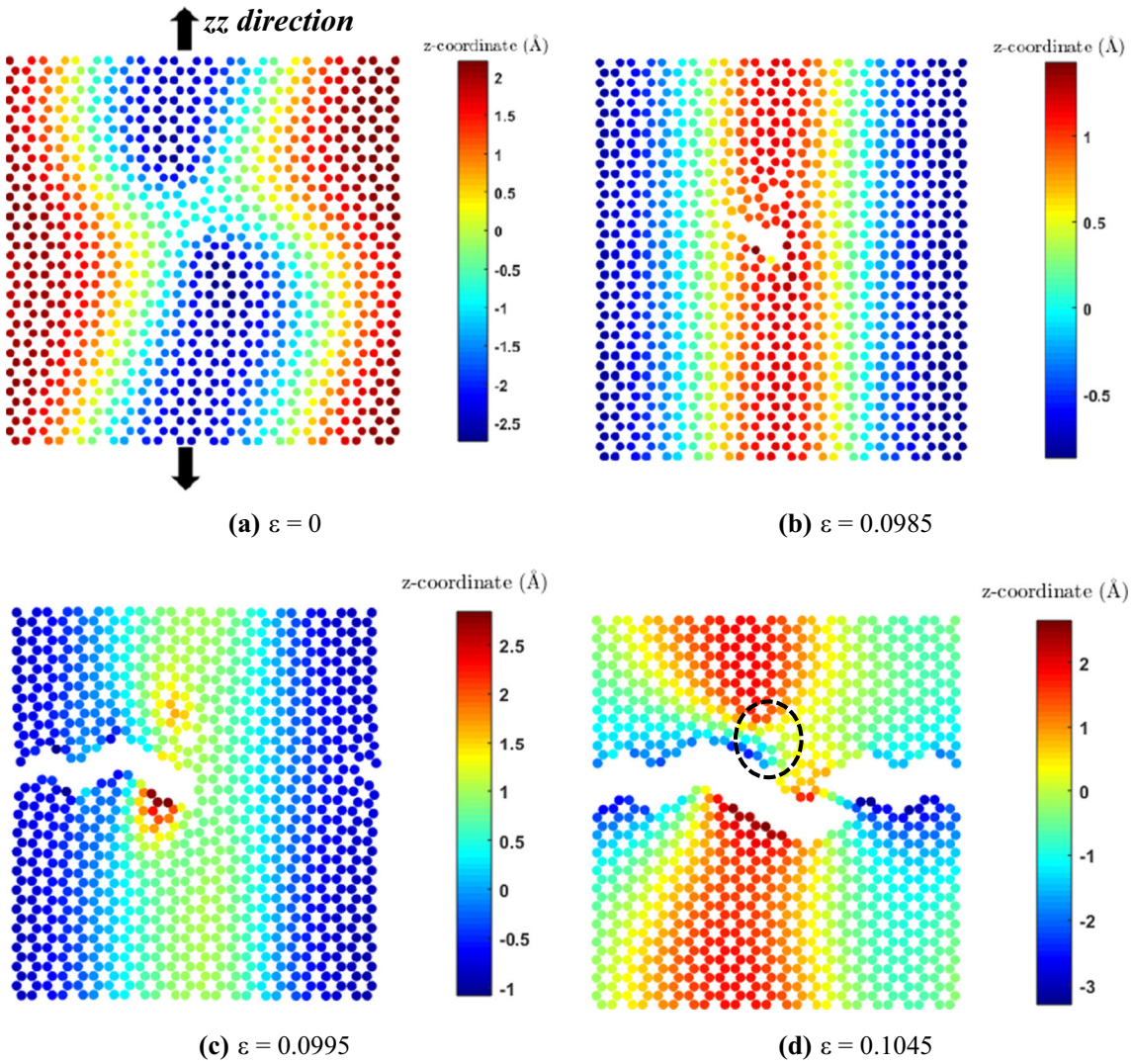

Fig. 14 Out-of-plane displacement considering the ELD 1 along the *zz* direction

with the loading direction with a crest along the defect line for ELD1 and troughs on both left and right sides. Further loading of ELD1 causes the bonds to break around the defect, and the crest region disappears. In the case of ELD3, the defect line shows minor out of plane displacements throughout loading, and the ripples are asymmetric about the defect line. Unlike those in *ar* direction, the fracture starts at the extremities of the line

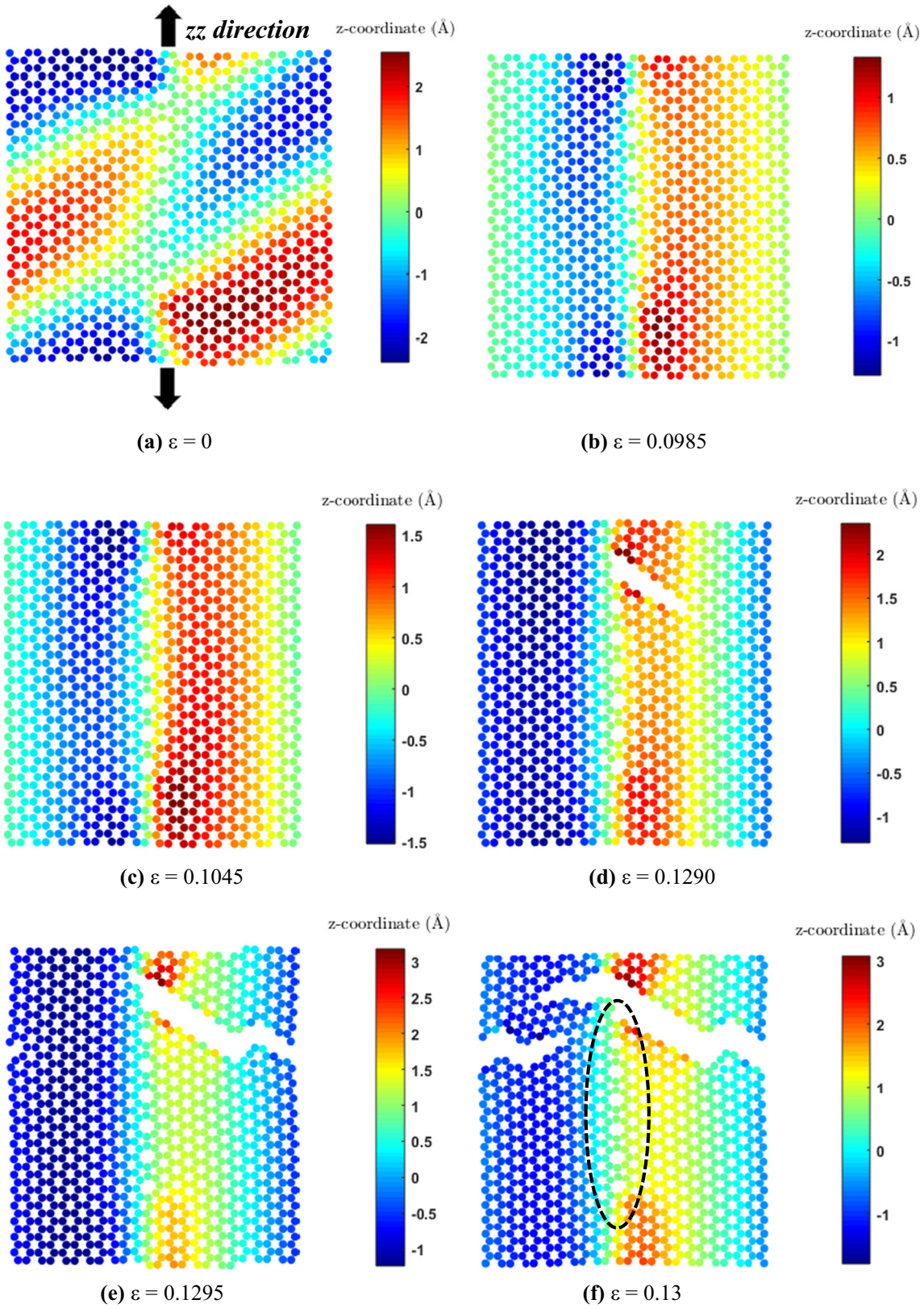

Fig. 15 Out-of-plane displacement considering the ELD 3 along the *zz* direction

defect by breaking the bonds shared by pentagon–octagon and octagon–hexagon cells, and then it propagates through the bonds shared by hexagons. Note that the extremities of the line defect have asymmetric edges with one pentagon, different from the inside of ELD where pairs of pentagons exist. Moreover, it is observed during the MD simulations that as the extremity of the ELD becomes symmetric the fracture behaviour becomes like a pristine zigzag sheet. Therefore, the mechanical response of sheets with ELDs for loading along the *zz* direction depends on the length of the line defect, and as closer the line of defect approaches the sheet edges, the defect has a smaller effect on the mechanical response. It is clear that the fracture force and pattern are strongly dependent on the length of grain boundary and defect density [33,45].

4 Conclusions

Accuracy of AFEM in estimating the tensile properties of graphene with complex topological defects has been established by a systematic comparison with MD simulations. Comparisons with MD solutions confirm that AFEM based on the second-generation REBO potential can capture the failure of graphene sheets with the fracture strength and strain slightly underestimated/overestimated ($\pm 10\%$). In general, the mechanical response of graphene shows a complex dependency on the defect shape, chirality, and loading direction. Armchair sheets with defects are generally weaker and less ductile compared to the zigzag sheets. The mechanical response of nanoporous graphene does not follow the size of the pore, instead it has a complex relationship with the pore size and the pore boundary atomic arrangement. The defect 5555-6-7777 shows the best mechanical behaviour compared to other defects in the *ar* direction, whereas SW1 defects are mechanically stronger in the *zz* direction compared to other defects. Moreover, it is concluded that the 5555-6-7777 defect can be introduced in graphene without compromising the stiffness in both *ar* and *zz* directions. Furthermore, the fracture behaviour of the armchair ELDs shows minor dependency on the length of the defect, whereas the length-effects are significant in the fracture behaviour of the zigzag ELDs changing it from brittle to ductile fracture. This study confirms that the AFEM is a potential tool for topological optimization and design studies of graphene as it is relatively faster compared to MD.

Acknowledgements This study was supported by grants from Natural Sciences and Engineering Research Council of Canada and São Paulo Research Foundation (Fapesp) funding for CEPID Process 2013/08293-7.

References

1. Lee, C., Wei, X., Kysar, J.W., Hone, J.: Measurement of the elastic properties and intrinsic strength of monolayer graphene. Science **321**(80), 385–388 (2008). https://doi.org/10.1126/science.1157996
2. Kim, K.S., Zhao, Y., Jang, H., Lee, S.Y., Kim, J.M., Kim, K.S., Ahn, J.-H., Kim, P., Choi, J.-Y., Hong, B.H.: Large-scale pattern growth of graphene films for stretchable transparent electrodes. Nature **457**, 706–10 (2009). https://doi.org/10.1038/nature07719
3. Chen, B.C., Hone, J.: Graphene Nanoelectromechanical Systems. Proc. IEEE. **101**, (2013)
4. Hu, Y., Shenderova, O.A., Hu, Z., Padgett, C.W., Brenner, D.W.: Carbon nanostructures for advanced composites. Rep. Prog. Phys. **69**, 1847–1895 (2006). https://doi.org/10.1088/0034-4885/69/6/R05
5. Fürst, J.A., Pedersen, J.G., Flindt, C., Mortensen, N.A., Brandbyge, M., Pedersen, T.G., Jauho, A.P.: Electronic properties of graphene antidot lattices. New J. Phys. **11**, 095020 (2009). https://doi.org/10.1088/1367-2630/11/9/095020
6. Surwade, S.P., Smirnov, S.N., Vlassiouk, I.V., Unocic, R.R., Veith, G.M., Dai, S., Mahurin, S.M.: Water desalination using nanoporous single-layer graphene. Nat. Nanotechnol. **10**, 459–464 (2015). https://doi.org/10.1038/nnano.2015.37
7. Yuan, W., Chen, J., Shi, G.: Nanoporous graphene materials. Mater. Today **17**, 77–85 (2014). https://doi.org/10.1016/j.mattod.2014.01.021
8. Stone, A.J., Wales, D.J.: Theoretical studies of icosahedral C60 and some related species. Chem. Phys. Lett. **128**, 501–503 (1986)
9. Lahiri, J., Lin, Y., Bozkurt, P., Oleynik, I.I., Batzill, M.: An extended defect in graphene as a metallic wire. Nat. Nanotechnol. **5**, 326–329 (2010). https://doi.org/10.1038/nnano.2010.53
10. Zhang, J., Zhao, J., Lu, J.: Intrinsic Strength and Failure Behaviors of Graphene Grain Boundaries. ACS Nano **6**, 2704–2711 (2012). https://doi.org/10.1021/nn3001356
11. Banhart, F., Kotakoski, J., Krasheninnikov, A.V.: Structural defects in graphene. ACS Nano **5**, 26–41 (2011). https://doi.org/10.1021/nn102598m
12. Rajasekaran, G., Narayanan, P., Parashar, A.: Effect of point and line defects on mechanical and thermal properties of graphene: a review. Crit. Rev. Solid State Mater. Sci. **41**, 47–71 (2016). https://doi.org/10.1080/10408436.2015.1068160
13. Kotakoski, J., Krasheninnikov, A.V., Kaiser, U., Meyer, J.C.: From point defects in graphene to two-dimensional amorphous carbon. Phys. Rev. Lett. **106**, 1–4 (2011). https://doi.org/10.1103/PhysRevLett.106.105505
14. Botello-Méndez, A.R., Declerck, X., Terrones, M., Terrones, H., Charlier, J.C.: One-dimensional extended lines of divacancy defects in graphene. Nanoscale **3**, 2868–2872 (2011). https://doi.org/10.1039/c0nr00820f

15. de Souza, F.A.L., Amorim, R.G., Prasongkit, J., Scopel, W.L., Scheicher, R.H., Rocha, A.R.: Topological line defects in graphene for applications in gas sensing. Carbon N. Y. **129**, 803–808 (2018). https://doi.org/10.1016/j.carbon.2017.11.029
16. Vicarelli, L., Heerema, S.J., Dekker, C., Zandbergen, H.W.: Controlling defects in graphene for optimizing the electrical properties of graphene nanodevices. ACS Nano **9**, 3428–3435 (2015). https://doi.org/10.1021/acsnano.5b01762
17. Ansari, R., Ajori, S., Motevalli, B.: Mechanical properties of defective single-layered graphene sheets via molecular dynamics simulation. Superlattices Microstruct. **51**, 274–289 (2012). https://doi.org/10.1016/j.spmi.2011.11.019
18. Malakouti, M., Montazeri, A.: Nanomechanics analysis of perfect and defected graphene sheets via a novel atomic-scale finite element method. Superlattices Microstruct. **94**, 1–12 (2016). https://doi.org/10.1016/j.spmi.2016.03.049
19. Dewapriya, M.A.N., Rajapakse, R.K.N.D.: Molecular dynamics simulations and continuum modeling of temperature and strain rate dependent fracture strength of graphene with vacancy defects. J. Appl. Mech. **81**, 081010 (2014). https://doi.org/10.1115/1.4027681
20. Liu, Y., Chen, X.: Mechanical properties of nanoporous graphene membrane. J. Appl. Phys. **115**, (2014). https://doi.org/10.1063/1.4862312
21. Lee, H.L., Wang, S.W., Yang, Y.C., Chang, W.J.: Effect of porosity on the mechanical properties of a nanoporous graphene membrane using the atomic-scale finite element method. Acta Mech. **228**, 2623–2629 (2017). https://doi.org/10.1007/s00707-017-1855-y
22. Jing, N., Xue, Q., Ling, C., Shan, M., Zhang, T., Zhou, X., Jiao, Z.: Effect of defects on Young's modulus of graphene sheets: a molecular dynamics simulation. RSC Adv. **2**, 9124–9129 (2012). https://doi.org/10.1039/c2ra21228e
23. Wang, S.P., Guo, J.G., Zhou, L.J.: Influence of Stone-Wales defects on elastic properties of graphene nanofilms. Phys. E. **48**, 29–35 (2013). https://doi.org/10.1016/j.physe.2012.11.002
24. Wang, M.C., Yan, C., Ma, L., Hu, N., Chen, M.W.: Effect of defects on fracture strength of graphene sheets. Comput. Mater. Sci. **54**, 236–239 (2012). https://doi.org/10.1016/j.commatsci.2011.10.032
25. He, L., Guo, S., Lei, J., Sha, Z., Liu, Z.: The effect of Stone-Thrower-Wales defects on mechanical properties of graphene sheets: a molecular dynamics study. Carbon N. Y. **75**, 124–132 (2014). https://doi.org/10.1016/j.carbon.2014.03.044
26. Wang, S., Yang, B., Yuan, J., Si, Y., Chen, H.: Large-scale molecular simulations on the mechanical response and failure behavior of a defective graphene: cases of 5–8-5 defects. Sci. Rep. **5**, 1–9 (2015). https://doi.org/10.1038/srep14957
27. Liu, B., Huang, Y., Jiang, H., Qu, S., Hwang, K.C.: The atomic-scale finite element method. Comput. Methods Appl. Mech. Eng. **193**, 1849–1864 (2004). https://doi.org/10.1016/j.cma.2003.12.037
28. Liu, B., Jiang, H., Huang, Y., Qu, S., Yu, M.F., Hwang, K.C.: Atomic-scale finite element method in multiscale computation with applications to carbon nanotubes. Phys. Rev. B. **72**, 035435 (2005). https://doi.org/10.1103/PhysRevB.72.035435
29. Cecchi, M.M., Rispoli, V., Venturin, M.: An atomic-scale finite element method for single-walled carbon nanotubes. Appl. Ind. Math. Italy III. **449–460**, (2009). https://doi.org/10.1142/9789814280303_0040
30. Damasceno, D.A., Mesquita, E., Rajapakse, R.K.N.D., Pavanello, R.: Atomic-scale finite element modelling of mechanical behaviour of graphene nanoribbons. Int. J. Mech. Mater. Des. **1–13**, (2018). https://doi.org/10.1007/s10999-018-9403-z
31. Gajbhiye, S.O., Singh, S.P.: Multiscale nonlinear frequency response analysis of single-layered graphene sheet under impulse and harmonic excitation using the atomistic finite element method. J. Phys. D Appl. Phys. **48**, 145305 (2015). https://doi.org/10.1088/0022-3727/48/14/145305
32. Brenner, D.W., Shenderova, O.A., Harrison, J.A., Stuart, S.J., Ni, B., Sinnott, S.B.: A second-generation reactive empirical bond order (REBO) potential energy expression for hydrocarbons. Mater. Sci. **14**, 783–802 (2002). https://doi.org/10.1088/0953-8984/14/4/312
33. Zhang, T., Li, X., Gao, H.: Fracture of graphene: a review. Int. J. Fract. **196**, 1–31 (2015). https://doi.org/10.1007/s10704-015-0039-9
34. Plimton, S.: Fast parallel algorithms for short-range molecular dynamics. J. Comput. Phys. **117**, 1–19 (1995). https://doi.org/10.1006/jcph.1995.1039
35. Kim, N.H.: Introduction to nonlinear finite element analysis. (2015)
36. Dewapriya, M.A.N.: Molecular Dynamics Study of Effects of Geometric Defects on the Mechanical Properties of Graphene. Master's thesis, University of British Columbia (2012)
37. Cao, G.: Atomistic studies of mechanical properties of graphene. Polymers (Basel). **6**, 2404–2432 (2014). https://doi.org/10.3390/polym6092404
38. Rajasekaran, G., Parashar, A.: Molecular dynamics study on the mechanical response and failure behaviour of graphene: performance enhancement via 5–7-7-5 defects. RSC Adv. **6**, 26361–26373 (2016). https://doi.org/10.1039/c6ra01762b
39. Li, M., Deng, T., Zheng, B., Zhang, Y., Liao, Y., Zhou, H.: Effect of defects on the mechanical and thermal properties of graphene. Nanomaterials. **9**, 347 (2019). https://doi.org/10.3390/nano9030347
40. Fan, N., Ren, Z., Jing, G., Guo, J., Peng, B., Jiang, H.: Numerical investigation of the fracture mechanism of defective graphene sheets. Materials (Basel). **10**, 1–12 (2017). https://doi.org/10.3390/ma10020164
41. Kochnev, A.S., Ovid'ko, I.A., Semenov, B.N.: Tensile strength of graphene containing 5-8-5 defects. Rev. Adv. Mater. Sci. **37**, 105–110 (2014)
42. Stehr, J., Buyanova, I., Chen, W.: Defects in Advanced Electronic Materials and Novel Low Dimensional Structures. Woodhead Publishing; 1 edn (2018)
43. Berger, D., Ratsch, C.: Line defects in graphene: How doping affects the electronic and mechanical properties. Phys. Rev. B. **93**, 235441 (2016). https://doi.org/10.1103/PhysRevB.93.235441
44. Humphrey, W., Dalke, A., Schulten, K.: VMD: Visual molecular dynamics. J. Mol. Graph. **14**, 33–38 (1996). https://doi.org/10.1016/0263-7855(96)00018-5
45. Wang, Y., Liu, Z.: Spontaneous rolling-up and assembly of graphene designed by using defects. Nanoscale. **10**, 6487–6495 (2018). https://doi.org/10.1039/c8nr00286j